The Astronomical Journal, 137:4561–4576, 2009 June doi:10.1088/0004-6256/137/6/4561

COLLISIONAL DEBRIS AS LABORATORIES TO STUDY STAR FORMATION

M. Boquien[1,2,10], P.-A. Duc[2], Y. Wu[3], V. Charmandaris[4,11], U. Lisenfeld[5], J. Braine[6], E. Brinks[7], J. Iglesias-Páramo[8], and C. K. Xu[9]

[1] University of Massachusetts, Department of Astronomy, LGRT-B 619E, Amherst, MA 01003, USA; boquien@astro.umass.edu
[2] AIM–Unité Mixte de Recherche CEA–CNRS–Université Paris VII–UMR n° 7158
[3] Astronomy Department, Cornell University, Ithaca, NY 14853, USA
[4] Department of Physics, University of Crete, GR-71003, Heraklion, Greece
[5] Department de Física Teórica y del Cosmos, Universidad de Granada, Granada, Spain
[6] Observatoire de Bordeaux, UMR 5804, CNRS/INSU, B.P. 89, F-33270 Floirac, France
[7] Centre for Astrophysics Research, University of Hertfordshire, College Lane, Hatfield AL10 9AB, UK
[8] Instituto de Astrofísica de Andalucía, Camino Bajo de Huétor 50, 18008 Granada, Spain
[9] California Institute of Technology, MC 405-47, 1200 East California Boulevard, Pasadena, CA 91125, USA
Received 2008 November 18; accepted 2009 March 18; published 2009 April 15

ABSTRACT

In this paper we address the question of whether star formation (SF) is driven by local processes or the large-scale environment. To do so, we investigate SF in collisional debris where the gravitational potential well and velocity gradients are shallower and compare our results with previous work on SF in noninteracting spiral and dwarf galaxies. We have performed multiwavelength spectroscopic and imaging observations (from the far-ultraviolet to the mid-infrared) of six interacting systems, identifying a total of 60 star-forming regions in their collision debris. Our analysis indicates that in these regions (1) the emission of the dust is at the expected level for their luminosity and metallicity, (2) the usual tracers of SFR display the typical trend and scatter found in classical star-forming regions, and (3) the extinction and metallicity are not the main parameters governing the scatter in the properties of intergalactic star-forming regions; age effects and variations in the number of stellar populations seem to play an important role. Our work suggests that local properties such as column density and dust content, rather than the large-scale environment seem to drive SF. This means that intergalactic star-forming regions can be used as a reliable tool to study SF.

Key words: galaxies: dwarf – galaxies: interactions – galaxies: irregular – infrared: galaxies – stars: formation – ultraviolet: galaxies

Online-only material: color figures

1. INTRODUCTION

With the launch of the *Spitzer* and *GALEX* space observatories, the study of star formation (SF) in galaxies has seen tremendous development. Several surveys have been dedicated to SF in the nearby universe. Among those, the *Spitzer* Infrared Nearby Galaxies Survey (SINGS; Kennicutt et al. 2003), the Local Volume Legacy Survey (LVL; Kennicutt et al. 2007), and the Nearby Galaxy Survey (NGS; Gil de Paz et al. 2007) have provided a large database of star-forming regions located in galaxies of various morphological types.

In galactic disks, SF is governed by complex processes that may depend on the local and large-scale environments. The underlying old stellar population can affect SF (Jog & Solomon 1984b, 1984a) modifying the stability of molecular clouds. Gas clouds may collapse and form stars under the effect of density waves (Lin & Shu 1964). In contrast, Galactic rotation provides a stabilizing effect (Toomre 1964). In general, the interplay between the large scale and local processes is still a puzzle. In that respect, the dwarf irregular galaxies studied as part of the NGS and LVL surveys may be interesting laboratories: they lack density waves making them simpler objects than more massive galaxies. However, they are less chemically evolved; the low metallicity of their interstellar medium introduces a local difference in the SF process, with respect to spiral disks, which makes a direct comparison difficult. The outermost regions of isolated spiral galaxies have recently become popular alternative targets (Braine & Herpin 2004; Thilker et al. 2005; Gil de Paz et al. 2005). Some systems show an ultraviolet (UV) excess, the origin of which has been strongly debated. These regions share the low metallicity of dwarf galaxies.

It is possible, however, to find at the same time a large-scale environment similar to that of dwarfs and the local properties of spirals, i.e., the debris of galaxy–galaxy interactions. This debris are located outside massive galactic disks, but consist of chemically enriched material expelled from parent galaxies: the metallicity of their gas is close to solar (see, for example, Figure 17 in Duc et al. 2000).[12] Furthermore, some metal-rich "intergalactic" regions may even be "pure," i.e., completely devoid of old stars, making them even less complex objects than typical dwarf galaxies.

Intergalactic star-forming regions, in spite of having been proposed by Zwicky (1956) and recognized as such by Schweizer (1978), have generated serious interest among astrophysicists for only about a decade. To put them better into context, intergalactic star-forming regions can be classified as:

1. Compact or diffuse emission-line regions, with no luminous stellar continuum (Weilbacher et al. 2003; Ryan-Weber

[10] CEA-Saclay, DSM/DAPNIA/Service d'Astrophysique, 91191 Gif-sur-Yvette CEDEX, France.
[11] IESL/Foundation for Research and Technology—Hellas, GR-71110, Heraklion, Greece and Chercheur Associé, Observatoire de Paris, F-75014, Paris, France.

[12] We use for the solar metallicity $12 + \log \mathrm{O/H} = 8.66$ (Asplund et al. 2005).

et al. 2004; Mendes de Oliveira et al. 2004; Cortese et al. 2006; Werk et al. 2008). These faint star-forming regions are not gravitationally bound and contribute to the chemical enrichment of the intergalactic medium.

2. Giant H II regions able to form young super star clusters, with masses between 10^6 $M_\odot$ and 10^7 $M_\odot$ (Weilbacher et al. 2003; de Grijs et al. 2003; López-Sánchez et al. 2004).
3. Tidal dwarf galaxies (TDG) (Duc & Mirabel 1994; Duc et al. 2000, 2007; Braine et al. 2000; Boquien et al. 2007, and references included in those papers), i.e., gravitationally bound objects with sizes and masses similar to those of dwarf galaxies. They usually contain large quantities of gas in atomic and molecular form (Hibbard et al. 1994; Braine et al. 2000, 2001; Lisenfeld et al. 2002, 2004).

Unlike SF in disks, SF in collisional debris may resemble "beads on a string" processes, which could be either stochastic (Smith et al. 2008), induced by gravitational instabilities (Elmegreen & Efremov 1996) or a result of shocks (Struck 1997).

To assess the potential of each of these processes, a preliminary study was performed by Boquien et al. (2007) on one system, NGC 5291, a very massive collisional ring hosting numerous star-forming regions. Here, we propose to extend this work to a larger sample of objects. Six additional interacting systems exhibiting prominent intergalactic star-forming regions were studied using multiwavelength UV to mid-infrared (MIR) data.

In Section 2, we present the selected systems, our PI and archival observations, and data reduction. In Section 3, we compare the properties of the star-forming regions in collisional debris to the more traditional process restricted to spiral galaxy disks. We discuss our results in Section 4.

2. OBSERVATIONS AND DATA REDUCTION

We have collected multiwavelength data on a limited sample of carefully selected colliding systems, presented here below.

2.1. Selected Systems

The goal of this paper is not to present a complete picture of intergalactic SF. The systems we have studied were mainly chosen based on the presence of prominent star-forming regions in their collisional debris. As shown later, they are not representative of the Local universe. Nevertheless, they offer the best laboratories where SF can be studied in detail in this environment. All of them benefit from extensive multiwavelength observations. In particular, they all have been observed in the UV by *GALEX* and in the MIR by *Spitzer*. Besides the space-borne data, ground-based spectrophotometry is available. A high oxygen abundance, typical of the outer regions of spiral disks (about half solar), has been measured in the H II regions throughout their collisional debris (Duc & Mirabel 1994, 1998; Duc et al. 2000, 2007). Despite common characteristics—active SF, high metallicity, environment—the six systems presented in this study turn out to present a variety of origins (early tidal interaction, ongoing and final merger, direct collision) and environments (field, groups and cluster of galaxies). For most of them, numerical simulations able to account for their perturbed morphology have already been performed. Details on individual systems are given below in their description. Additional details are summarized in Table 1. Optical images of all systems are shown in Figures 1–6.

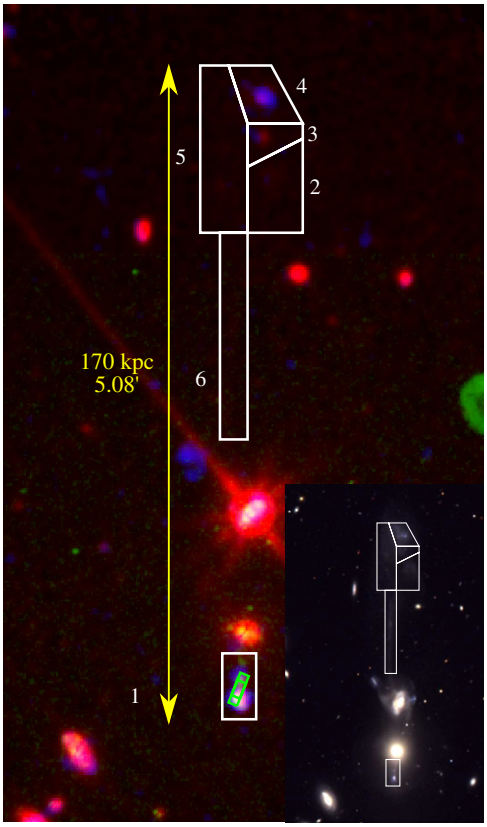

Figure 1. Arp 105 seen at 8.0 μm (red; including the dust and the stellar emission), Hα (green), and FUV (blue). North is up; east is left. The numbered white polygons are the apertures in which the fluxes have been measured. The green rectangles are the positions of the IRS slit. Inset image: optical BVR image taken at the CFHT 3.6 m/12 k.

(A color version of this figure is available in the online journal.)

Table 1
Position and Distance of the Selected Systems

System	R.A. (J2000)	Decl. (J2000)	Distance (Mpc)	Spatial Resolution for 1″ (pc)
Arp 105	$11^h11^m13\overset{s}{.}1$	$+28°41'57''$	115	557.5
Arp 245	$09^h45^m45\overset{s}{.}3$	$-14°20'50''$	31	150.3
NGC 5291	$13^h47^m24\overset{s}{.}5$	$-30°24'25''$	62	300.6
NGC 7252	$22^h20^m44\overset{s}{.}8$	$-24°40'42''$	64	310.3
Stephan Quintet	$22^h35^m57\overset{s}{.}5$	$+33°57'36''$	85	412.1
VCC 2062	$12^h48^m00\overset{s}{.}0$	$+10°58'15''$	17	82.4

Note. The coordinates have been obtained from the NASA/IPAC Extragalactic Database (NED).

2.1.1. Arp 105

Arp 105 (NGC 3561) is the result of an ongoing collision between a spiral and an elliptical. This interaction has given birth to several tidal features: a 100 kpc long tidal arm (regions 2 to 6) to the north with knots of SF at its tip (regions 3 and 4) apparently embedded in a low surface brightness older stellar structure, and a jet-like tail passing in front of the elliptical, ending (region 1) with a gas-rich, blue object (Duc & Mirabel 1994; Duc et al. 1997). This young TDG has the morphology of a Blue Compact Dwarf Galaxy (BCDG), while having an Interstellar Medium (Oxygen and CO rich) more typical of a spiral galaxy.

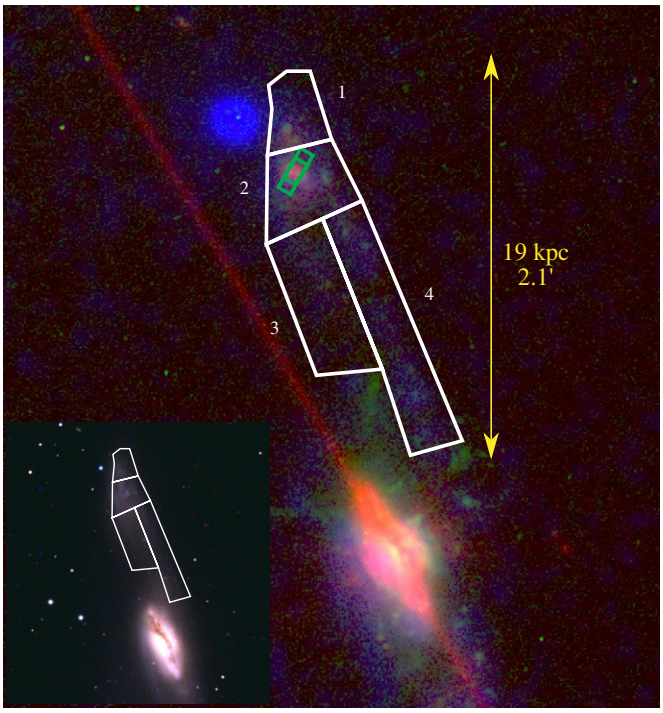

Figure 2. Arp 245 seen at 8.0 μm (red; including the dust and the stellar emission), Hα (green), and FUV (blue). North is up; east is left. The numbered white polygons are the apertures in which the fluxes have been measured. The green rectangles are the positions of the IRS slit. Inset image: optical BVR image taken at ESO La Silla NTT/EMMI.

(A color version of this figure is available in the online journal.)

2.1.2. Arp 245

Arp 245 (NGC 2992/93) is the result of an ongoing collision between two spiral galaxies, connected by an apparent bridge (Duc et al. 2000). The tidal tail (regions 1 to 4) north of NGC 2992 ends (regions 1 and 2) with a star-forming complex where abundant molecular gas has been found (Braine et al. 2000). The color of the tail outside the star-forming regions (regions 3 and 4) indicates the presence of an old underlying stellar population.

2.1.3. NGC 5291

NGC 5291 provides an example of a spectacular collisional ring around an early-type galaxy, probably resulting from the head-on, high-speed, collision with a massive companion within a cluster of galaxies (Bournaud et al. 2007). The giant (180 kpc diameter), gas-rich, ring contains a string of metal-rich star-forming regions (Duc & Mirabel 1998). The most luminous of them, in which CO lines Braine et al. (2001) and Polycyclic Aromatic Hydrocarbon (PAH) dust bands Higdon et al. (2006) were detected, are located within gravitationally bound, rotating, substructures with the mass of dwarf galaxies (Bournaud et al. 2007). Its intergalactic star-forming regions were studied in detail by Boquien et al. (2007). In this paper we present new *GALEX* far-ultraviolet (FUV) data.

A new FUV image is presented in Figure 3. See also Figures 1 and 2 in Boquien et al. (2007). The two brightest clumps, NGC 5291S and NGC 5291N correspond to regions 3 and 21.

2.1.4. NGC 7252

NGC 7252 is the archetypal example of an advanced merger of two spiral galaxies, observed between 5×10^8 and 10^9 years after the initial collision (Hibbard & Mihos 1995). Each of its two tidal tails hosts one blue star-forming TDG at its end. The one in the east contains two weak star-forming regions (regions 3 and 4) whereas the northwest tail contains the brightest one (region 1).

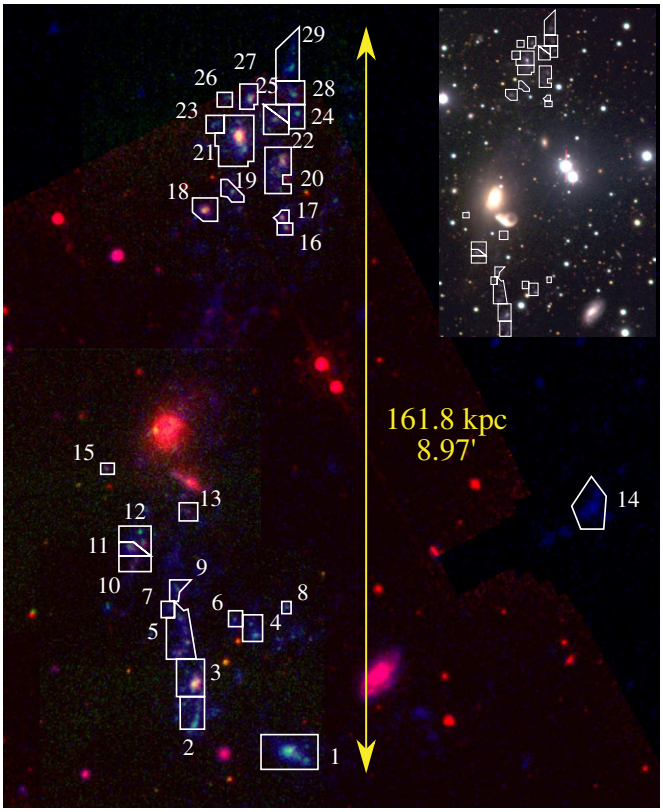

Figure 3. NGC 5291 seen at 8.0 μm (red; including the dust and the stellar emission), Hα (green), and FUV (blue). North is up; east is left. The numbered white polygons are the apertures in which the fluxes have been measured. Inset image: optical BVR image taken at ESO La Silla NTT/EMMI.

(A color version of this figure is available in the online journal.)

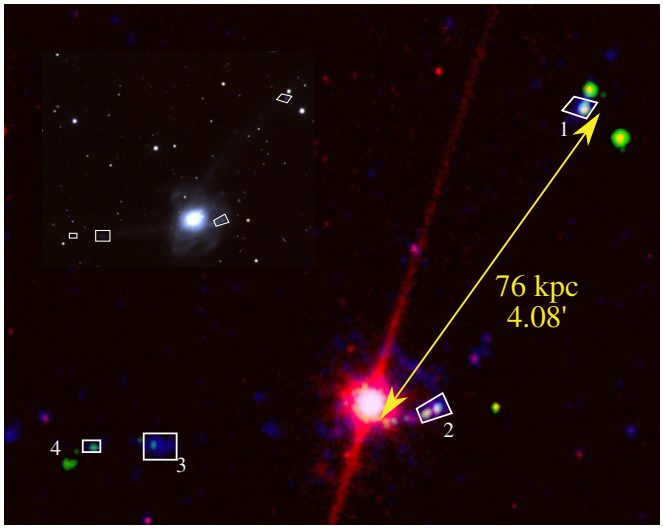

Figure 4. NGC 7252 seen at 8.0 μm (red; including the dust and the stellar emission), Hα (green), and FUV (blue). North is up; east is left. The numbered white polygons are the apertures in which the fluxes have been measured. Inset image: optical BVR image taken at ESO La Silla NTT/EMMI.

(A color version of this figure is available in the online journal.)

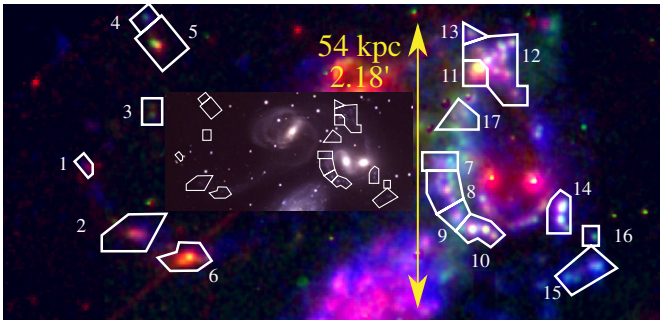

Figure 5. Stephan's Quintet seen at 8.0 μm (red; including the dust and the stellar emission), Hα (green), and FUV (blue). North is up; east is left. The numbered white polygons are the apertures in which the fluxes have been measured. Inset image: optical BVR image taken at Calar Alto 3.5 m/MOSCA.

(A color version of this figure is available in the online journal.)

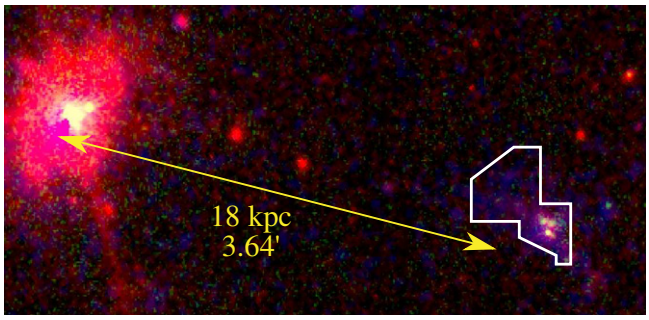

Figure 6. VCC 2062 seen at 8.0 μm (red; including the dust and the stellar emission), Hα (green), and FUV (blue). North is up; east is left. The white polygon is the aperture in which the fluxes have been measured.

(A color version of this figure is available in the online journal.)

2.1.5. Stephan's Quintet

Stephan's Quintet is a well-known compact group of galaxies that have suffered interactions of various types.

1. Tidal interactions, responsible for the formation of several tails, one particularly faint and old, another, more prominent, hosting a dust enshrouded, molecule-rich, star-forming object (SQ-B; Lisenfeld et al. 2002) (region 6) with another star-forming region at its tip (region 2), and a recent one, made of pure atomic gas which has condensed locally to form faint but compact knots of SF, regions 3–5 (Mendes de Oliveira et al. 2004).
2. Violent shocks due to an intruding galaxy which hit the system at a line of sight speed of 1000 km s^{-1}. These are thought to lie at the origin of Hα and X-ray filaments where also prominent MIR molecular H_2 lines have been detected (Appleton et al. 2006), regions 7–10 and 17). The shock region is most likely devoid of young stars and is excluded from this analysis. However, a luminous star-forming region known as SQ-A (regions 11–13), with PAH emission, has developed at its boundary.

Other intergalactic star-forming regions are detected southwest of the system in regions 14 to 16.

2.1.6. VCC 2062

Finally, VCC 2062 provides in the nearby universe an example of a well resolved TDG, which is likely the result of an old merger Duc et al. (2007). Located in the Virgo cluster, it is linked to its putative parent galaxy, NGC 4694, by an H I arm which only shows an optical counterpart at the location of the dwarf galaxy. VCC 2062 exhibits several H II regions within a low surface brightness stellar body. Its high oxygen abundance and strong CO detection is inconsistent with it being a classical dwarf galaxy.

2.2. Reference Sample

The properties of the individual star-forming regions within collisional debris have been systematically compared to those located in the disks of four spirals. This broadband reference sample consists of the following galaxies. (1) M51, a well studied spiral galaxy located at 8.2 Mpc (see for instance Calzetti et al. 2005), (2) M81, the main galaxy of the M81 group, located at 3.63 Mpc; its star-forming regions have been studied by Pérez-González et al. (2006), (3) Arp 24, an interacting system at 27.6 Mpc which hosts massive star clusters studied by Cao & Wu (2007), and (4) Arp 82, an interacting system at 57 Mpc exhibiting a long tidal arm containing multiple star forming knots, as illustrated in Hancock et al. (2007).

While Arp 24 and Arp 82 are interacting systems, they are still in an early phase. Contrary to all objects in the primary list, SF still mainly occurs in the galaxy under the "classical" regime and not along a tidal tail. This explains why they are included in the reference sample.

Since the most luminous star-forming objects in collisional debris have the luminosities of dwarf galaxies, it is also relevant to make a comparison with the *integrated*, broadband properties of individual galaxies. Large reference samples are available. In this study we made use of the following ones: (1) the 75 spiral galaxies of the SINGS survey (Kennicutt et al. 2003; Dale et al. 2007), (2) the 19 dwarf galaxies with $M_B > -19$ from the sample by Rosenberg et al. (2006), and (3) the 66 starburst galaxies from the sample by Engelbracht et al. (2008).

As we also study the MIR spectral properties of tidal debris we have gathered several samples having *Spitzer* Infrared Spectrograph (IRS) observations, namely (1) galaxies from the BCDG sample of Wu et al. (2006), (2) the starburst sample of Engelbracht et al. (2008), and (3) individual star-forming regions in M101 (Gordon et al. 2008).

2.3. Imaging

Three star-forming tracers—the UV, Hα, and MIR emission—were used for the present study. Their observation is described here and summarized in Table 2.

2.3.1. Ultraviolet Imaging

All UV images were obtained using the *GALEX* space telescope. It offers 2 bands, FUV ($\lambda_{\rm eff}$ = 151 nm) and NUV ($\lambda_{\rm eff}$ = 227 nm) and a large field of view of 1.°24. NGC 5291 observations were obtained through our *GALEX* program (PID 32). An NUV image of the system was presented in Boquien et al. (2007). The FUV image which was not available at the time is now included in this paper. Maps of other systems where obtained from the NGS survey. Note that the Arp 105 image was taken by the *GALEX* All-Sky Imaging Survey and therefore the exposure time was limited to 115 s, instead of at least 500 s, as for the other systems. Due to the low photon count in UV, the sky histogram closely follows a Poisson distribution and the quantization is seen very clearly. To determine the sensitivity we have fitted the sky background histogram with a Poisson distribution of the form : $f(k;\lambda) = \lambda^k \exp(-\lambda)/k!$, where k is the number of

Table 2
Summary of Available Imaging Observations for the Selected Systems

System	Type	Instrument	Band	Source
Arp 105	Imaging	*GALEX*	FUV	Archive
”	”	”	NUV	”
”	Imaging	*Spitzer* IRAC	3.6 μm	Archive
”	”	”	4.5 μm	”
”	”	”	8.0 μm	”
”	Fabry-Perot Imaging	CFHT 3.6m/MOS/FP	Hα	PI, Bournaud et al. (2004)
Arp 245	Imaging	*GALEX*	FUV	Archive
”	”	”	NUV	”
”	Imaging	*Spitzer* IRAC	3.6 μm	Archive
”	”	”	4.5 μm	”
”	”	”	8.0 μm	”
”	Narrowband Imaging	La Silla NTT/EMMI	Hα	PI, Bournaud et al. (2004)
NGC 5291	Imaging	*GALEX*	FUV	GI PID 32, Boquien et al. (2007)
”	”	”	NUV	”
”	Imaging	*Spitzer* IRAC	3.6 μm	Archive, Boquien et al. (2007)
”	”	”	4.5 μm	”
”	”	”	8.0 μm	”
”	Fabry-Perot Imaging	La Silla 3.6m/CIGALE	Hα	PI, Bournaud et al. (2004)
NGC 7252	Imaging	*GALEX*	FUV	Archive
”	”	”	NUV	”
”	Imaging	*Spitzer* IRAC	3.6 μm	Archive
”	”	”	4.5 μm	”
”	”	”	8.0 μm	”
”	Narrowband imaging	KPNO	Hα	Archive
SQ	Imaging	*GALEX*	FUV	archive, Xu et al. (2005)
”	”	”	NUV	”
”	Imaging	*Spitzer* IRAC	3.6 μm	Archive
”	”	”	4.5 μm	”
”	”	”	8.0 μm	”
”	Narrowband imaging	Calar Alto 2.1 m	Hα	PI, Xu et al. (1999)
VCC 2062	Imaging	*GALEX*	FUV	PI, Duc et al. (2007)
”	...	”	NUV	”
”	Imaging	*Spitzer* IRAC	3.6 μm	Archive
”	”	”	4.5 μm	”
”	”	”	8.0 μm	”
”	Narrowband imaging	KPNO	Hα	Archive, Duc et al. (2007)

photons and λ the variance. In the case the photon count is high enough to have a normal distribution, we have used the MSKY procedure[13] to obtain the sensitivity per pixel. We have converted to a sensitivity per arcsec^2 multiplying by the pixel scale (1.″5 per pixel). The exposure times and the sensitivities for each band are summarized in Table 3.

2.3.2. Hα Imaging

Hα images were obtained using Fabry–Perot (FP) and narrowband observations obtained at various ground based telescopes (see Table 2). The reconstructed FP images were flux calibrated using the narrowband images as well as slit spectroscopy. See Boquien et al. (2007) for details.

The exposure times and the sensitivities for each band are summarized in Table 4. The sensitivities have been calculated using MSKY. The sensitivity could not be measured for NGC 7252. Indeed for this system, only archival Hα images for which the background has been removed are available.

[13] MSKY is an IRAF routine written by M. Dickinson (1993, private communication). It allows one to define the interval in the pixel distribution where the mode and the variance are calculated.

Table 3
Summary of the UV Observations of the Selected Systems

System	Band	Exposure Time (s)	1σ sensitivity (μJy arcsec^{-2})
Arp 105	FUV	115	0.10
”	NUV	”	0.10
Arp 245	FUV	1052	0.05
”	NUV	4298	0.03
NGC 5291	FUV	5567	0.03
”	NUV	2886	0.02
NGC 7252	FUV	562	0.05
”	NUV	”	0.05
SQ	FUV	3322	0.05
”	NUV	”	0.04
VCC 2062	FUV	1530	0.03
”	NUV	”	0.03

2.3.3. Mid-Infrared Imaging

All infrared observations were taken from the *Spitzer* space telescope archives. For our systems, only images at 3.6, 4.5, 5.8, and 8.0 μm from the Infrared Array Camera (IRAC) were available. The MIPS 24 μm images of NGC 7252 and VCC 2062 are too shallow to be of use in this study.

Table 4
Summary of the Hα Observations of the Selected Systems

System	Exposure Time (s)	1σ Sensitivity (μJy arcsec^{-2})
Arp 105	300	3.3×10^{-21}
Arp 245	900	5.7×10^{-21}
NGC 5291	180–255	2.2×10^{-21}
NGC 7252	1200	...
SQ	600	3.4×10^{-21}
VCC 2062	1200	3.0×10^{-21}

Table 5
Summary of the Mid-Infrared Observations of the Selected Systems

System	Band	Exposure Time (s)	1σ Sensitivity (μJy arcsec^{-2})
Arp 105	3.6 μm	450	0.12
"	4.5 μm	"	0.17
"	8.0 μm	"	1.29
Arp 245	3.6 μm	300	0.48
"	4.5 μm	"	0.56
"	8.0 μm	"	1.96
NGC 5291	3.6 μm	432	0.27
a "	4.5 μm	"	0.30
"	8.0 μm	"	1.10
NGC 7252	3.6 μm	120	0.23
"	4.5 μm	"	0.31
"	8.0 μm	"	1.31
SQ	3.6 μm	432	0.20
"	4.5 μm	"	1.11
"	8.0 μm	"	1.11
VCC 2062	3.6 μm	120	0.20
"	4.5 μm	"	0.25
"	8.0 μm	"	1.49

The images were retrieved from the archives and processed (cosmic ray rejection, interpolation, mosaicking, etc.) using the standard IRAC pipeline. Due to the presence of strong gradients in the 5.8 μm images that would have made flux measurements particularly uncertain, they have not been used in this study. The sensitivities were calculated using MSKY. The exposure times and the sensitivities for each band are summarized in Table 5.

The stellar emission from the 8.0 μm fluxes has not been subtracted. The main reason why any stellar subtraction was not attempted was that such a correction applied to intergalactic regions would increase the errors rather than reducing them. Indeed, these regions were chosen to have specifically a high SFR and a low background old stellar population. The stellar continuum subtraction is usually done using the IRAC 3.6 μm band. Assuming a [3.6]–[8.0] = 0 color for the stars, as in Pahre et al. (2004), the stellar contribution to the 8.0 μm flux is expected to be at about 7% for our objects. However, in luminous SF regions the IRAC 3.6 μm band may be significantly polluted by the 3.3 μm PAH line. This contribution is very uncertain as the line wavelength is too short to be observed with IRS. Taking this into account, we have decided not to correct the 8.0 μm flux for the stellar contribution.

2.3.4. Aperture Photometry

Aperture photometry was carried out on a number of selected star-forming regions in each system. All images had previously been registered to a common grid. The standard selection of the star-forming regions is based on the presence of UV, Hα, and UV emission.

The apertures are defined to enclose as few star-forming regions as possible in order to limit the number of stellar populations. The aim is to keep the star-forming regions simple. Indeed the presence of an increasing number of stellar populations renders the study more complex. The limiting factor to define the apertures is the resolution of the infrared and UV images. To take into account the variety of resolutions we define the apertures taking into account all images simultaneously.

The background level is defined by averaging typically 5 to 20 measurements of the background around each star-forming region. In case it is not possible to measure the background for each region individually[14], the same background level is defined for a set of regions. The number of regions is kept as small as possible in order to limit the influence of any large-scale background variability.

The procedure how the regions were selected and apertures defined is described in detail in Boquien et al. (2007). The selected apertures are displayed in Figures 1–6.

The measured fluxes are listed in Tables 6 to 11.

2.4. Mid-Infrared Spectroscopy

Unpublished archival *Spitzer*/IRS MIR spectroscopic observations are presented here of two TDG candidates in Arp 105 and Arp 245. These observations were carried out using the Short–Low (SL: 5.2–14.5 μm; $R = 64 \sim 128$) and Short–High (SH: 9.9–19.6 μm; $R = 600$) modules of the Infrared Spectrograph (IRS; Houck et al. 2004). Arp 105S and Arp 245N were observed for three cycles of 60 s in the SL mode and three cycles of 120 s in the SH mode on 2005 December 12 and on 2005 May 30, respectively. The data were processed with the *Spitzer* Science Center (SSC) pipeline version S13.0.1. The reduction started from the intermediate pipeline products (droop files), which only lacked stray light and flat-field correction. Individual points to each nod position of the slit were coadded using median averaging. Sky background from the SL spectral data was taken out by differencing the images of the two orders in this module. Then the differenced images were extracted with the spectral modeling, analysis, and reduction tool (SMART; Higdon et al. 2004) using a variable width aperture, which scales the extraction aperture with wavelength to recover the same fraction of the diffraction-limited instrumental point-spread function. The SH data were extracted with the full slit extraction method in SMART. Finally, the spectra were flux-calibrated by multiplying by the relative spectral response function (RSRF), which was created from the IRS standard stars αLac for SL and ξDra for SH for which accurate templates are available (Cohen et al. 2003). The SL spectra are presented in Figure 7 for Arp 105S (corresponding to region 1 in Figure 1) and 8 for Arp 245N (corresponding to region 2 in Figure 2)

In Tables 12 and 13, we present the measurements of broad and narrow emission-line features from the IRS spectra of Arp 105S and Arp 245N. We have also measured the equivalent width (EW) of NGC 5291N and NGC 5291S independently of Higdon et al. (2006). Indeed, this allows an easier comparison with the data of Wu et al. (2006) whose EWs have been measured using the same method. The EW of the PAH features are measured from the SL spectra. The PAH EW were derived by integrating the flux of the feature in the mean spectra of both

[14] This happens generally when the star-forming regions are too close to each other.

Table 6
Ultraviolet, Infrared, and Hα Fluxes for the Selected Regions of Arp 105

Region	F_{FUV} (μJy)	F_{NUV} (μJy)	$F_{3.6\ \mu m}$ (μJy)	$F_{4.5\ \mu m}$ (μJy)	$F_{8.0\ \mu m}$ (μJy)	$F_{H\alpha}$ (10^{-19} W m^{-2})
1	58 ± 3	105 ± 7	489 ± 192	348 ± 129	2564 ± 712	276 ± 2
2	1 ± 5	9 ± 12	440 ± 46	270 ± 57	334 ± 151	...
3	5 ± 3	9 ± 5	200 ± 17	130 ± 21	373 ± 56	...
4	28 ± 4	72 ± 8	620 ± 30	390 ± 37	871 ± 97	...
5	0 ± 6	12 ± 16	730 ± 59	470 ± 73	662 ± 195	...
6	8 ± 8	41 ± 20	860 ± 76	490 ± 94	442 ± 251	...

Notes. The fluxes have not been corrected for Galactic extinction. The *Spitzer* IRS observation of Arp 105S is best associated with region 1.

Table 7
Ultraviolet, Infrared, and Hα Fluxes for the Selected Regions of Arp 245

Region	F_{FUV} (μJy)	F_{NUV} (μJy)	$F_{3.6\ \mu m}$ (μJy)	$F_{4.5\ \mu m}$ (μJy)	$F_{8.0\ \mu m}$ (μJy)	$F_{H\alpha}$ (10^{-19} W m^{-2})
1	24 ± 2	46 ± 1	1350 ± 31	810 ± 59	2540 ± 194	73 ± 8
2	54 ± 3	93 ± 2	3630 ± 51	2200 ± 99	9140 ± 325	212 ± 13
3	15 ± 4	42 ± 3	3360 ± 74	2120 ± 144	2980 ± 476	96 ± 19
4	41 ± 5	69 ± 3	3510 ± 93	2270 ± 182	4530 ± 601	145 ± 24

Notes. The fluxes have not been corrected for Galactic extinction. The *Spitzer* IRS observation of Arp 245N is best associated with region 2.

Table 8
Ultraviolet, Infrared, and Hα Fluxes for the Selected Regions of NGC 5291

Region	F_{FUV} (μJy)	F_{NUV} (μJy)	$F_{3.6\ \mu m}$ (μJy)	$F_{4.5\ \mu m}$ (μJy)	$F_{8.0\ \mu m}$ (μJy)	$F_{H\alpha}$ (10^{-19} W m^{-2})
1	255 ± 18	274 ± 20	331 ± 102	254 ± 35	640 ± 99	332 ± 101
2	82 ± 6	92 ± 7	144 ± 41	98 ± 24	629 ± 41	107 ± 33
3	134 ± 10	160 ± 12	385 ± 24	251 ± 32	2088 ± 56	188 ± 57
4	44 ± 4	53 ± 4	131 ± 13	118 ± 16	207 ± 28	43 ± 13
5	86 ± 7	98 ± 8	221 ± 28	179 ± 36	805 ± 64	59 ± 19
6	13 ± 1	14 ± 2	31 ± 6	28 ± 7	97 ± 13	15 ± 5
7	11 ± 1	14 ± 2	53 ± 12	44 ± 5	73 ± 12	6 ± 3
8	6 ± 1	6 ± 1	31 ± 7	31 ± 3	60 ± 7	10 ± 4
9	20 ± 2	23 ± 2	84 ± 15	61 ± 7	176 ± 16	15 ± 5
10	11 ± 1	14 ± 2	112 ± 27	95 ± 10	278 ± 27	14 ± 5
11	30 ± 3	34 ± 3	199 ± 18	138 ± 8	384 ± 19	25 ± 9
12	28 ± 3	31 ± 3	229 ± 34	169 ± 13	509 ± 34	43 ± 13
13	10 ± 1	12 ± 2	188 ± 19	135 ± 8	311 ± 19	13 ± 5
14	57 ± 5	62 ± 5	...	...	...	...
15	4 ± 1	5 ± 1	70 ± 9	50 ± 5	189 ± 10	8 ± 4
16	12 ± 1	14 ± 2	50 ± 11	41 ± 6	286 ± 12	14 ± 5
17	13 ± 1	12 ± 1	52 ± 9	37 ± 6	377 ± 11	13 ± 5
18	27 ± 2	30 ± 3	146 ± 29	104 ± 13	1047 ± 30	33 ± 10
19	16 ± 2	18 ± 2	96 ± 19	51 ± 8	267 ± 19	16 ± 5
20	73 ± 6	87 ± 7	287 ± 59	244 ± 22	1428 ± 59	78 ± 25
21	218 ± 16	259 ± 19	638 ± 39	534 ± 52	5236 ± 90	463 ± 139
22	25 ± 2	30 ± 3	63 ± 27	34 ± 16	427 ± 28	21 ± 7
23	14 ± 2	17 ± 2	14 ± 18	...	114 ± 17	15 ± 5
24	21 ± 2	21 ± 2	2 ± 21	25 ± 11	31 ± 20	19 ± 7
25	12 ± 1	15 ± 2	38 ± 13	30 ± 8	235 ± 14	12 ± 5
26	7 ± 1	9 ± 1	...	...	...	7 ± 3
27	36 ± 3	44 ± 4	115 ± 23	100 ± 14	614 ± 24	42 ± 13
28	30 ± 3	33 ± 3	...	...	...	23 ± 9
29	38 ± 3	41 ± 4	...	...	...	25 ± 9

Notes. The fluxes have not been corrected for Galactic extinction. The *Spitzer* IRS observation of NGC 5291S (respectively NGC 5291N) is best associated with region 3 (respectively 21).

nod positions above an adopted continuum and then dividing by the average adopted continuum. The baseline was determined by fitting a spline function to selected points. The wavelength limits for the integration of the features were approximately 5.95–6.55 μm for the 6.2 μm PAH, 7.15–8.20 μm for the 7.7 μm PAH, 8.20–8.90 μm for the 8.6 μm PAH and 10.80–11.80 μm

Table 9
Ultraviolet, Infrared, and Hα Fluxes for the Selected Regions of NGC 7252

Region	$F_{\rm FUV}$ (μJy)	$F_{\rm NUV}$ (μJy)	$F_{3.6\,\mu{\rm m}}$ (μJy)	$F_{4.5\,\mu{\rm m}}$ (μJy)	$F_{8.0\,\mu{\rm m}}$ (μJy)	$F_{\rm H\alpha}$ (10^{-19} W m^{-2})
1	32 ± 2	32 ± 2	138 ± 31	87 ± 24	946 ± 50	93 ± 47
2	36 ± 4	40 ± 13	221 ± 256	194 ± 126	1082 ± 636	55 ± 28
3	23 ± 2	28 ± 3	113 ± 26	83 ± 22	231 ± 92	5 ± 3
4	4 ± 1	5 ± 1	14 ± 7	16 ± 7	41 ± 26	9 ± 5

Note. The fluxes have not been corrected for Galactic extinction.

Table 10
Ultraviolet, Infrared, and Hα Fluxes for the Selected Regions of Stephan's Quintet

Region	$F_{\rm FUV}$ μJy	$F_{\rm NUV}$ μJy	$F_{3.6\,\mu{\rm m}}$ μJy	$F_{4.5\,\mu{\rm m}}$ μJy	$F_{8.0\,\mu{\rm m}}$ μJy	$F_{\rm H\alpha}$ 10^{-19} W m^{-2}
1	2 ± 1	2 ± 1	31 ± 10	15 ± 5	225 ± 17	...
2	16 ± 2	19 ± 2	215 ± 58	127 ± 32	1192 ± 110	45 ± 35
3	2 ± 1	1 ± 1	18 ± 4	6 ± 11	167 ± 35	23 ± 11
4	4 ± 1	4 ± 1	3 ± 3	0 ± 9	99 ± 29	14 ± 9
5	3 ± 1	4 ± 1	40 ± 13	33 ± 4	780 ± 53	92 ± 31
6	8 ± 1	11 ± 1	396 ± 5	279 ± 19	3541 ± 65	149 ± 22
7*	40 ± 8	51 ± 8	457 ± 123	215 ± 134	896 ± 254	431 ± 14
8*	61 ± 15	82 ± 14	928 ± 225	459 ± 245	1613 ± 465	578 ± 25
9*	33 ± 7	43 ± 7	326 ± 103	161 ± 112	689 ± 212	308 ± 12
10*	48 ± 11	60 ± 11	639 ± 171	329 ± 185	2100 ± 352	576 ± 19
11	19 ± 4	23 ± 6	550 ± 159	360 ± 86	3736 ± 228	540 ± 12
12	124 ± 15	139 ± 24	987 ± 732	476 ± 397	5246 ± 1051	959 ± 55
13	10 ± 2	10 ± 3	10 ± 76	21 ± 33	283 ± 109	56 ± 6
14	72 ± 8	74 ± 4	444 ± 457	192 ± 277	1654 ± 287	399 ± 18
15	60 ± 5	60 ± 5	144 ± 188	77 ± 150	391 ± 203	177 ± 30
16	5 ± 2	5 ± 2	89 ± 41	50 ± 33	82 ± 45	36 ± 7
17*	26 ± 3	28 ± 5	74 ± 146	56 ± 140	776 ± 164	488 ± 17

Notes. The fluxes have not been corrected for Galactic extinction. The entries marked with an asterisk indicate shocked regions.

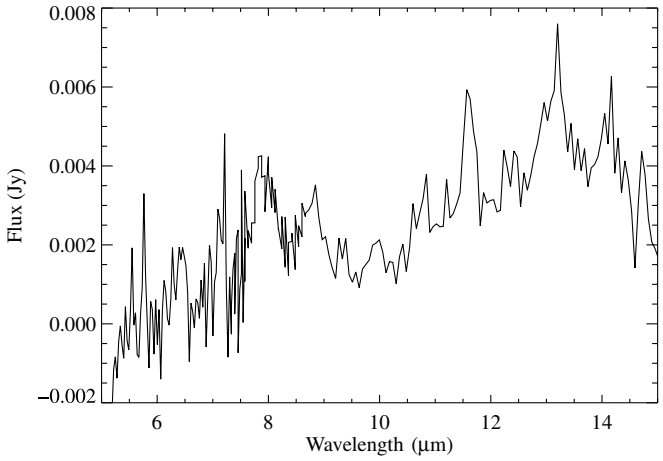

Figure 7. 5–15 μm low-resolution spectrum of ARP 105S obtained with *Spitzer*/IRS. The strong PAH bands at 6.1, 7.7, 8.6, and 11.2 μm are visible. No rest-frame correction has been performed.

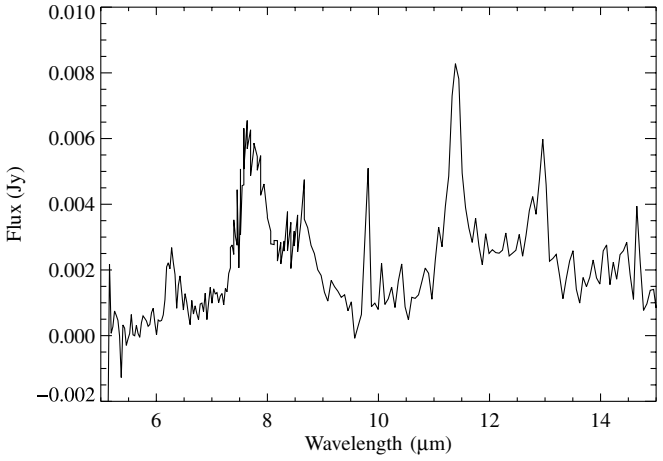

Figure 8. 5–15 μm low-resolution spectrum of ARP 245S obtained with *Spitzer*/IRS. The strong PAH bands at 6.1, 7.7, 8.6, and 11.2 μm are visible. No rest-frame correction has been performed.

for the 11.2 μm PAH features. The integrated fluxes for the fine structure lines of [S IV] 10.51 μm, [Ne II] 12.81 μm, [Ne III] 15.55 μm, and [S III] 18.71 μm were measured by fitting a Gaussian profile using the line-fitting function in SMART. Note that no sky background has been subtracted from the SH spectra. This has not affected our measurements of the spectral lines, however.

Table 11
Ultraviolet, Infrared, and Hα Fluxes for the Selected Regions of VCC 2062

Region	$F_{\rm FUV}$ μJy	$F_{\rm NUV}$ μJy	$F_{3.6\,\mu{\rm m}}$ μJy	$F_{4.5\,\mu{\rm m}}$ μJy	$F_{8.0\,\mu{\rm m}}$ μJy	$F_{\rm H\alpha}$ 10^{-19} W m^{-2}
1	35 ± 3	46 ± 4	210 ± 52	185 ± 55	1597 ± 387	42 ± 15

Note. The fluxes have not been corrected for Galactic extinction.

Table 12
Measured EW of the Most Prominent PAH Bands

Region	$EW_{6.2\ \mu m}$ (μm)	$EW_{7.7\ \mu m}$ (μm)	$EW_{11.2\ \mu m}$ (μm)
Arp 105S	0.865 ± 0.473	0.756 ± 0.249	0.245 ± 0.109
Arp 245N	1.312 ± 0.621	0.726 ± 0.175	0.884 ± 0.285
NGC 5291N	0.569 ± 0.068	0.349 ± 0.017	0.574 ± 0.053
NGC 5291S	0.550 ± 0.244	0.383 ± 0.079	0.780 ± 0.225

3. RESULTS

As shown in Figures 1–6, the UV, Hα and 8 μm maps of our selected interacting systems match well spatially, tracing the presence of a global process: SF. However, within a given system, large fluctuations may be found in the relative fluxes from one individual region to the other, indicating local differences. Since by far the most complex and ambiguous tracer of SF is the MIR emission, we detail in the following the dust properties of the collisional debris.

3.1. Dust in Collisional Debris

Mid-infrared PAH emission at 8.0 μm is observed within all the collisional debris of our sample; it is enhanced in or close to H II regions, as traced by the Hα maps.

PAH bands in collisional debris have been directly detected for the first time in the NGC 5291 system (Higdon et al. 2006). The new MIR spectra of the TDG candidates in Arp 105S and Arp 245N presented in this paper also exhibit strong PAH emission (see Figures 7 and 8), a property which may result from their relatively high metallicity. It has been established (e.g., Engelbracht et al. 2005; Walter et al. 2007, references there in) that the PAH emission is correlated with metallicity. In Figure 9 (respectively 10), we plot the 6.2 μm (respectively 11.2 μm) band EW of the PAH features versus oxygen abundance. Galaxies from the sample of Wu et al. (2006) and individual star-forming regions in the spiral M101 (Gordon et al. 2008) are plotted.

These plots show a clear correlation between the strength of the PAH emission and metallicity for the BCDGs and the M101 individual star-forming regions. The four intergalactic star-forming regions exhibit an aromatic emission at the expected level. Indeed, at a given metallicity, the EWs of the PAH bands emitted by the intergalactic star-forming regions are very similar to those of star-forming regions within galaxies.

As shown for instance by Madden et al. (2006), the strength of the PAH features is also closely connected with the hardness of the radiation field. Gordon et al. (2008) recently claimed that this parameter, itself correlated with metallicity (see Figure 11), is the main parameter governing the evolution of the strength of the PAH features. Indeed, lower metallicity stars emit harder radiation due to the lack of metals in their atmosphere. As a result, the hard radiation field combined with a high luminosity density can destroy PAH carriers (Wu et al. 2006).

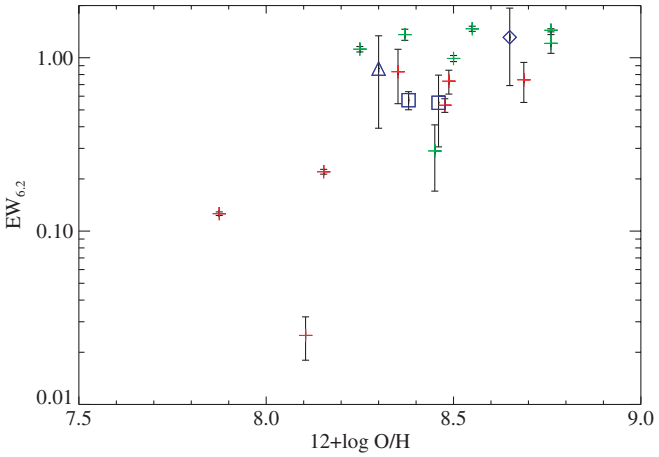

Figure 9. EW of the 6.2 μm PAH line vs. oxygen abundance in the intergalactic star-forming regions observed with the IRS (blue triangle for Arp 105S, diamond for Arp 245N, and squares for NGC 5291). The BCDGs from the Wu et al. (2006) sample (red crosses), and the individual star-forming regions in M101 (Gordon et al. (2008), green crosses) are plotted as well.

(A color version of this figure is available in the online journal.)

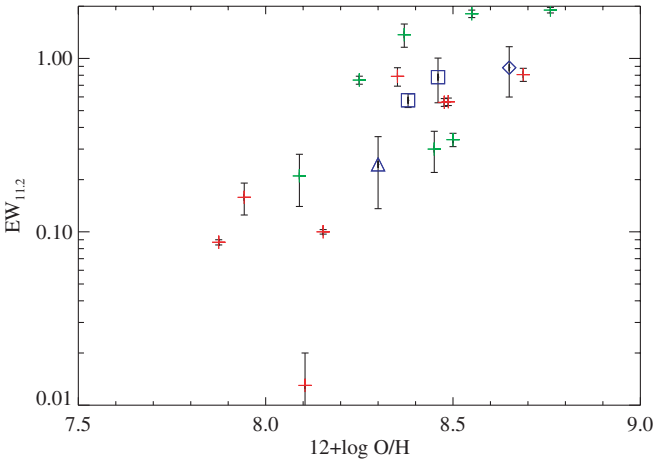

Figure 10. EW of the 11.2 μm PAH line vs. oxygen abundance in the intergalactic star-forming regions observed with the IRS. The color and shape of the symbols used is the same as in Figure 9.

(A color version of this figure is available in the online journal.)

Since we also have high-resolution IRS spectra for most regions in our sample we examine in Figures 12 and 13 the correlation between the neon line ratio and the EW of the 6.2 μm and 11.2 μm features. We find that the regions in the collisional debris fall broadly within the trend discussed by, e.g., Wu et al. (2006).

Unfortunately MIR spectra are available for only four TDGs. For the other collisional debris, we have used the emission in the IRAC 8.0 μm band as an indirect tracer. The validity of this approach has been discussed in more detail by several authors (see, e.g., Engelbracht et al. 2005, 2008) and is corroborated by our current results. In our IRS sample, PAH features dominate

Table 13
IRS Fluxes of Mid-Infrared Ionic Lines

Region	$F_{[S\ IV]@10.51\ \mu m}$ (10^{-18} W m^{-2})	$F_{[Ne\ II]@12.81\ \mu m}$ (10^{-18} W m^{-2})	$F_{[Ne\ III]@15.55\ \mu m}$ (10^{-18} W m^{-2})	$F_{[S\ III]@18.71\ \mu m}$ (10^{-18} W m^{-2})
Arp 105S	5.41 ± 1.16	4.71 ± 0.58	9.47 ± 0.44	9.49 ± 2.47
Arp 245N	...	4.19 ± 1.21	5.24 ± 0.48	4.99 ± 0.61

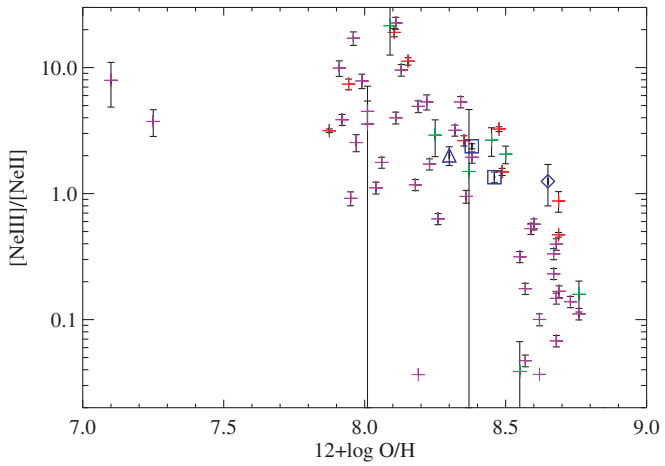

Figure 11. [Ne III]/[Ne II], a tracer of the hardness of the radiation field, vs. the oxygen abundances. Galaxies from the BCDG sample of Wu et al. (2006) (red crosses), from the starburst sample of Engelbracht et al. (2008) (purple crosses); individual star-forming regions in M101 (green crosses), and the intergalactic star-forming regions (blue triangle for Arp 105S, diamond for Arp 245N, and squares for NGC 5291).

(A color version of this figure is available in the online journal.)

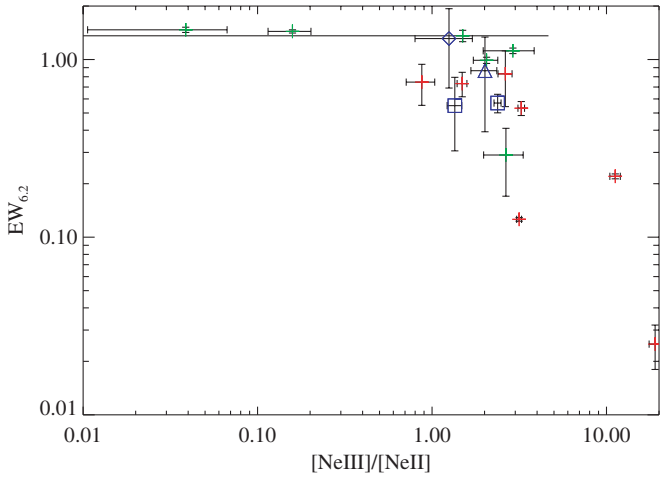

Figure 12. EW of the PAH 6.2 μm band as a function of the [Ne III]/[Ne II] ratio. The color and shape of the symbols used is the same as in Figure 9.

(A color version of this figure is available in the online journal.)

the emission in this broadband. Continuum emission from hot dust may, however, have a significant contribution which should be taken into account. To that purpose, we have adopted the method presented in Engelbracht et al. (2005, 2008): the 8.0 μm emission is normalized to the underlying hot dust continuum as follows: $F_{8.0}/(F_{4.5} - \alpha F_{3.6})$. This assumes that the 3.6 μm emission is purely stellar,[15] and that the IRAC 4.5 μm band traces the hot dust, once the stellar continuum has been subtracted. The value of α—the conversion factor from the 3.6 μm to the 4.5 μm stellar flux—is given by a spectral synthesis code and depends on the metallicity. For those intergalactic H II regions for which no oxygen abundance has yet been determined, we adopt $\alpha = 0.535$, the mean of the coefficients for the $8.15 \leqslant Z < 8.50$ and $8.50 \leqslant Z < 8.85$ bins from Engelbracht et al. (2008).

[15] In fact this band is also polluted by the 3.3 μm PAH feature as we mentioned earlier. Unfortunately, its strength may not be directly determined, even in the TDGs with mid-IR spectroscopic data: the IRS instrument does not cover this short wavelength range.

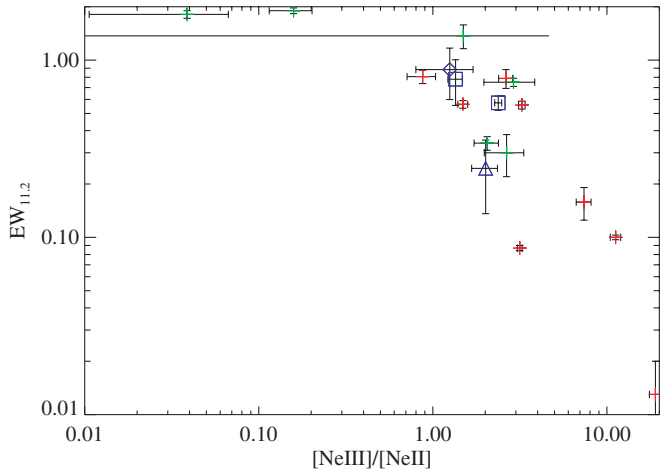

Figure 13. EW of the PAH 11.2 μm band as a function of the [Ne III]/[Ne II] ratio. The color and shape of the symbols used is the same as in Figure 9.

(A color version of this figure is available in the online journal.)

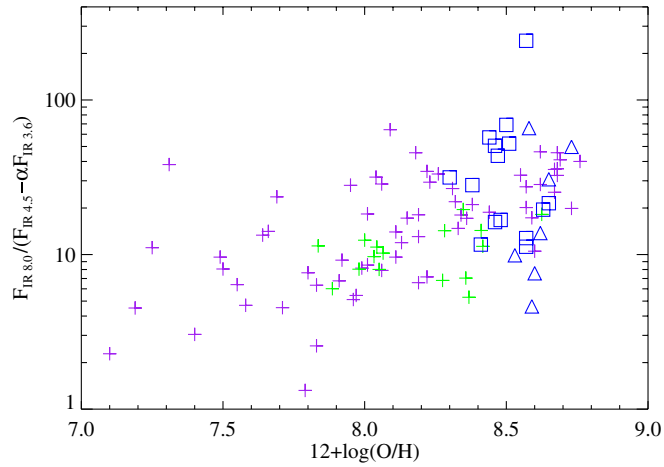

Figure 14. Ratio of the MIR fluxes $F_{8.0}/(F_{4.5} - \alpha F_{3.6})$ as a function of the oxygen abundance. Intergalactic star-forming regions are sorted in two categories whether they contain a significant old stellar population (blue triangles) or they are located within mainly gaseous streams (blue squares). Galaxies in the reference samples: Rosenberg et al. (2006) (green plusses), Engelbracht et al. (2008) (purple plusses).

(A color version of this figure is available in the online journal.)

In Figure 14, we plot the ratio of the MIR fluxes $F_{8.0}/(F_{4.5} - \alpha F_{3.6})$ as a function of oxygen abundance for intergalactic star-forming regions and the Rosenberg et al. (2006) dwarf galaxies, and the Engelbracht et al. (2008) starburst galaxies comparison samples. The aim is to see if intergalactic star-forming regions follow the same well-known relation between the strength of the aromatic emission and metallicity. This plot confirms that intergalactic star-forming regions lie along the correlation between the mid-IR emission, corrected for the hot dust and stellar contribution, and metallicity. The intergalactic star-forming regions seem to follow the same trend as spiral galaxies, although the dispersion might be slightly higher. This may also be seen in Figures 15 and 16 showing the $F_{8.0}/(F_{4.5} - \alpha F_{3.6})$ PAH indicator as a function of the 8.0 μm luminosity for the reference samples. The intergalactic star-forming regions describe approximately the upper envelope of the reference sample of integrated galaxies but the mean ratio is similar.

From this study of the dust properties of collisional debris, we conclude that their MIR emission, dominated by PAH, is "normal" and comparable to that of the star-forming regions in

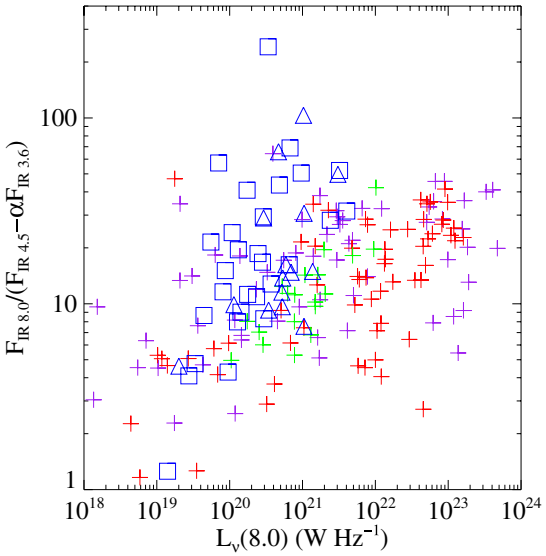

Figure 15. PAH fluxes traced by the 8.0 μm emission normalized to the underlying hot dust continuum $F_{8.0}/(F_{4.5}-\alpha F_{3.6})$ as a function of the 8.0 μ luminosity. Intergalactic star-forming regions are sorted in two categories whether they contain a significant old stellar population (blue triangles) or they are located within mainly gaseous streams (blue squares). Galaxies in the reference samples: SINGS (red plusses), Rosenberg et al. (2006) (green plusses), and Engelbracht et al. (2008) (purple plusses).

(A color version of this figure is available in the online journal.)

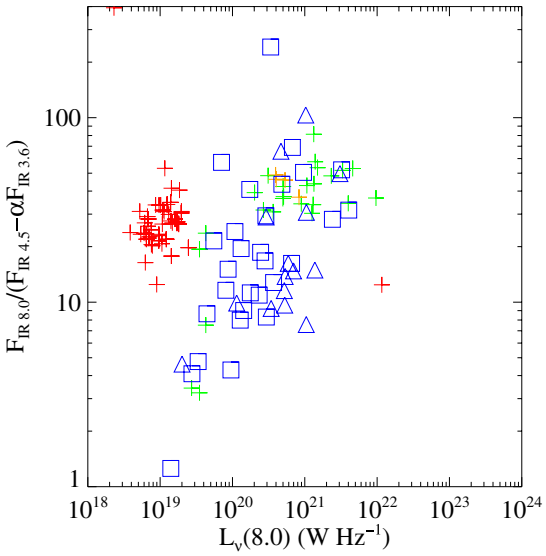

Figure 16. PAH fluxes traced by the 8.0 μm emission normalized to the underlying hot dust continuum $F_{8.0}/(F_{4.5}-\alpha F_{3.6})$ as a function of the 8.0 μm luminosity. Intergalactic star-forming regions are sorted in two categories whether they contain a significant old stellar population (blue triangles) or they are located within mainly gaseous streams (blue squares). Galactic star-forming regions in the reference samples: M81 (red plusses), Arp 82 (green plusses), and Arp 24 (orange plusses).

(A color version of this figure is available in the online journal.)

regular galaxies that have the same metallicity. PAH are emitted in photodissociation regions associated with SF episodes and are thus considered as a reliable tracer of SF (except in a low-Z environment; Calzetti et al. 2007). Thus the calibrations between the IRAC 8.0 μm band and the SFR, as determined for regular spiral galaxies, should also be valid for collisional debris. This assessment is exploited in the rest of the paper.

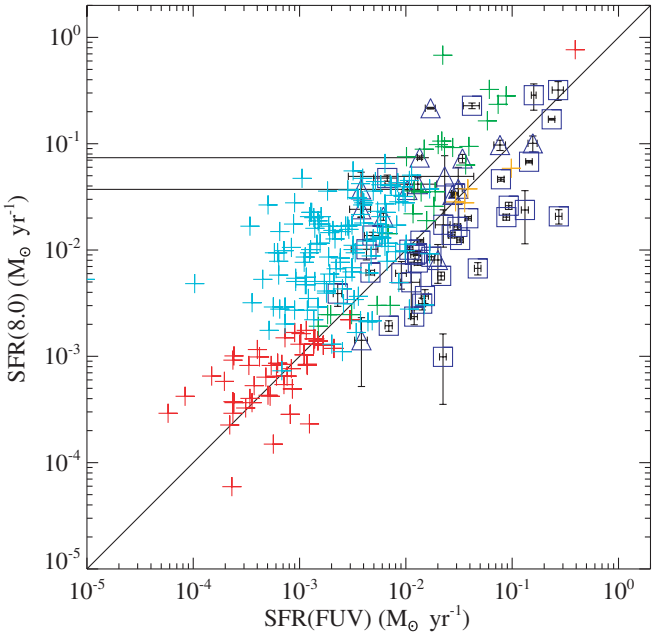

Figure 17. Comparison of the foreground Galactic extinction corrected SFR estimated from FUV and 8.0 μm. Intergalactic star-forming regions are sorted in two categories whether they contain a significant old stellar population (blue triangles) or they are located within mainly gaseous streams (blue squares). Galaxies in the reference samples: M 51 (turquoise plusses), M 81 (red plusses) and Arp 82 (green plusses). The black solid line indicates when the FUV derived and the 8.0 μm SFRs are identical.

(A color version of this figure is available in the online journal.)

3.2. Comparing Star Formation Rates

We compare here the emission of the three SF tracers used in this study. (1) UV emission, due to the direct radiation of mostly massive stars, (2) Hα emission from regions ionized by young, very massive stars, and (3) MIR 8.0 μm emission due to the PAHs in photodissociation regions.

These tracers, although all somehow related to the SF process, have their own characteristics and biases, which are discussed in Section 4.2.

To put the UV, Hα, and MIR luminosities on a common scale, we have converted them into units corresponding to measures of the SFR, using the following formulas:

1. SFR(UV) $= 1.4 \times 10^{-21} L_\nu$ [W Hz^{-1}].
2. SFR(Hα) $= 7.9 \times 10^{-35} L(H\alpha)$ [W].
3. SFR(8.0 μm) $= 1.88 \times 10^{-36} \nu L_\nu$ [W Hz^{-1}].

These conversion factors are based on the values determined by Kennicutt (1998) for the UV and Hα luminosities, and Wu et al. (2005) for the 8.0 μm emission. One should note that they are only valid for specific SF histories, in particular a SFR which is assumed to be constant for 100 Myr and with a Salpeter initial mass function (IMF). As discussed in Section 4.2.3, these conditions may not apply to collisional debris, and thus the derived SFR may be off by some unknown factor, especially in the youngest regions. This scaling is done here mainly to facilitate comparison between the three tracers (i.e., their fluxes) and to compare the SFR in debris with that of other star-forming regions.

In Figure 17 (respectively 18) we compare the SFR (uncorrected for extinction) estimated from the FUV band with that estimated from the 8.0 μm (respectively Hα). Boquien et al. (2007) have shown that the intergalactic SF regions around NGC 5291 exhibit a strong, systematic, UV excess that can

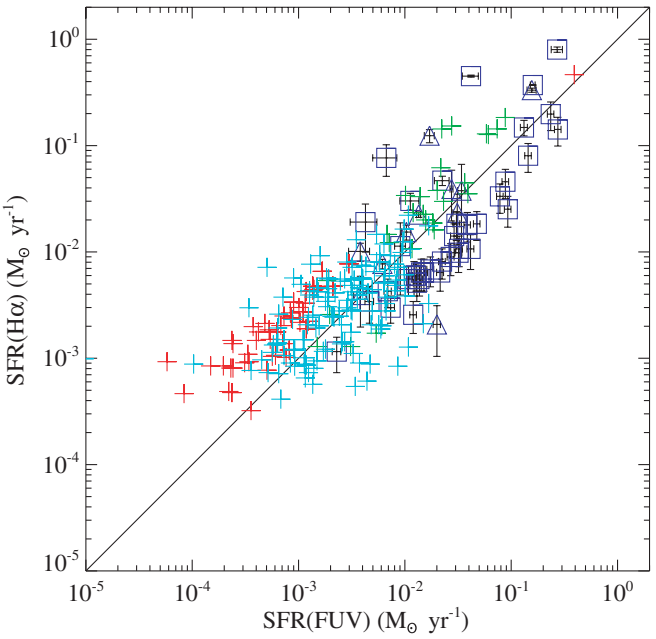

Figure 18. Comparison of the foreground Galactic extinction corrected SFR estimated from FUV and Hα. The color and shape of the symbols used is the same as in Figure 17.

(A color version of this figure is available in the online journal.)

Table 14
Total SFR in the Selected Star Forming Regions, Therefore Excluding Parent Galaxies, According to the Three Tracers: FUV, Hα, and Infrared at 8.0 μm

Sample	SFR(FUV) ($M_\odot$ yr^{-1})	SFR(Hα) ($M_\odot$ yr^{-1})	SFR(8.0) ($M_\odot$ yr^{-1})
Stephan's Quintet	0.71 ± 0.08	$> 2.08 \pm 0.10$	1.06 ± 0.14
Arp 105	0.28 ± 0.08	0.37 ± 0.002	0.59 ± 0.16
Arp 245	0.03 ± 0.002	0.05 ± 0.006	0.15 ± 0.01
NGC 5291	1.44 ± 0.10	$> 0.71 \pm 0.22$	$> 0.54 \pm 0.02$
NGC 7252	0.08 ± 0.01	0.07 ± 0.03	0.08 ± 0.03
VCC 2062	0.002 ± 0.0002	0.001 ± 0.0004	0.004 ± 0.0009
Rosenberg	...	...	0.14
SINGS	0.41	...	1.86
M 51	0.48	0.54	2.08
M 81	0.39	0.47	0.77
Arp 82	0.61	1.31	2.60
Arp 24	0.20	...	0.15

Notes. In the case of the Rosenberg et al. (2006) and SINGS samples, it is the SFR integrated over the entire object. The SFRs of the reference samples are computed with the same conversion factor as for the intergalactic star-forming regions, using the published luminosities.

be clearly seen in Figure 18 where Hα appears depressed compared to the FUV emission. On average, this is not the case in the other interacting galaxies in our sample (see Tables 14 and 15). This UV excess is found only locally, in specific star-forming regions, which mostly are hosted by gas-rich collisional debris. The dispersion among different regions is important, but not dramatically larger than that measured in star-forming regions belonging to a single galaxy, like M51. The 8.0 μm emission is itself the strongest for regions which contain an old stellar population. This is probably due to the fact that older stars can also heat the dust and therefore create diffuse emission. This kind of emission is particularly visible in spiral galaxies and can account for a significant fraction of the 8.0 μm flux as suggested by Calzetti et al. (2007).

4. DISCUSSION

4.1. The Star Formation Rate in Tidal Debris

The objects in our primary list were selected for having prominent star-forming regions in their collisional debris. This may be quantified using the UV maps, a reliable tracer of recent SF episodes. Table 16 lists the UV fluxes, converted to $M_\odot$ yr^{-1} (using the relation given in Section 3.2), from regions located within the optical radius of the parent galaxies and outside it, within the collisional debris. The instantaneous fraction of stars born in the "intergalactic" medium is as high as 80% with a median value of nearly 21%. The SFR in this environment may exceed 1 $M_\odot$ yr^{-1}, a value which corresponds to the measure of the SFR integrated over the entire disk of normal spiral galaxies! This SF is rate is a lower bound as it is not corrected for internal extinction.[16] Even if the extinction may be higher in spiral galaxies than in intergalactic star-forming regions, Boquien et al. (2007) showed that using the 8.0 μm indicator, the intergalactic SFR still accounted for over 50% of the total SFR in NGC 5291.

For comparison, in less active (and more typical) nearby interacting systems, the tidal structures account for 10% at most of the total SFR (Struck 2007; Smith et al. 2007; Hancock et al. 2007). Their result, uncorrected for extinction, holds whether the systems are observed in infrared, Hα, or UV.

One of the main characteristics of the collisional debris studied here is their high gas content, reflecting the fact that their parent galaxies were gas rich. This situation is rather rare in the local universe but was much more common at high redshift when galaxies had higher gas fractions.

4.2. Factors Affecting the Inferred SFR

This paper makes use of three SFR diagnostics that are sensitive to a number of factors.

1. *Timescale*: Hα is sensitive to the most recent SF (nearly instantaneous compared to UV), giving an estimate of the SFR averaged over a few million years. On the other hand UV emission gives an estimate of the SFR averaged over about 100 Myr,
2. *Metallicity*: the relation between PAH luminosity and SFR is not linear and depends on the metallicity. The Hα luminosity is also metal-dependent, as shown by Bicker & Fritze-v. Alvensleben (2005),
3. *Extinction*: UV radiation suffers the most from extinction ($A_{\rm FUV}/A_{\rm H\alpha} \sim 3.1$),
4. *Geometric factors*: Hα is sensitive to the effects of geometry. Young stars are enshrouded in dust clouds and their ionizing radiation is efficiently absorbed by dust, and
5. *Variations of the initial mass function*: depending on the distribution of the mass of stars at birth, the amount of energetic radiation emitted per unit mass changes. Since UV emission is not only due to the most massive stars, changes in the shape of the IMF will affect differently the UV and Hα luminosities.

In principle, ages, extinction, or even the IMF of a region of SF may be constrained by measuring flux ratios of UV/[8.0] or UV/Hα, when coupled with evolutionary synthesis models. In practice, strong degeneracies make this exercise particularly delicate.

[16] Spectroscopic observations necessitate long exposure times to observe all the selected star-forming regions in all the systems. In addition the use of the H I column density to evaluate the extinction is impaired by the lack of high resolution observations for some of the systems.

Table 15
Mean Ratio Between the PAH Emission and the Dust Continuum; Mean Ratio Between the SFR Estimated from the 8.0 μm Emission and from the FUV Emission and Mean Ratio of the SFR Estimated from the Hα Emission and from the FUV Emission

Sample	$\langle F_{8.0}/(F_{4.5}-\alpha F_{3.6})\rangle$	$\langle$SFR (8.0) /SFR (FUV)$\rangle$	$\langle$SFR (Hα) /SFR (FUV)$\rangle$
Stephan's Quintet	84 ± 74	3.0 ± 3.7	4.3 ± 3.8
Arp 105	16 ± 8	3.6 ± 3.5	...
Arp 245	20 ± 11	4.7 ± 1.5	1.8 ± 0.6
NGC 5291	17 ± 14	0.5 ± 0.3	0.4 ± 0.1
NGC 7252	24 ± 28	0.8 ± 0.5	0.8 ± 0.6
VCC 2062	21	1.7	0.5
Debris with older stars	26.0 ± 27.3	3.6 ± 3.6	1.9 ± 1.9
Debris without older stars	29.9 ± 46.7	1.0 ± 1.5	1.4 ± 2.5
Rosenberg	13 ± 8	...	...
SINGS	16 ± 11	9.6 ± 26.8	...
Engelbracht	20 ± 11	...	...
M 51	...	7.2 ± 9.0	1.7 ± 1.8
M 81	33 ± 48	1.4 ± 1.1	3.2 ± 2.0
Arp 82	36 ± 17	3.8 ± 5.7	2.0 ± 1.4
Arp 24	45 ± 5	0.8 ± 0.2	...

Note. Aberrant points are removed before calculating the above values. Those were due to regions having a very low ($F_{4.5} - \alpha F_{3.6}$) flux.

Table 16
SFR in the Intergalactic Medium, Total SFR in the System and Fraction of Stars Currently Formed in the Intergalactic Medium

System	SFR_{IGM}(FUV) ($M_\odot$ yr^{-1})	SFR_{total}(FUV) ($M_\odot$ yr^{-1})	SFR_{IGM}(FUV)/SFR_{total}(FUV)
Stephan's Quintet	0.71	3.41	20.8
Arp 105	0.28	0.64	43.2
Arp 245	0.03	1.33	2.5
NGC 5291	1.44	1.69	85.1
NGC 7252	0.08	0.73	11.3
VCC 2062	0.002	0.043	4.6

The aim here is to find which factors can explain the apparent diversity of intergalactic star-forming regions. This is particularly important to better understand the SF process in tidal debris and find what parameter is the driving factor. In this section, we verify the influence of the extinction, metallicity, or stellar populations. We have made here such a comparison between the various SF indicators for about 60 individual star-forming regions in collisional debris. We discuss below the effect of each parameter on the measure of the SFR, or more precisely on the scatter of the various estimates from one region to the other (see Section 3.2); we will try to determine which parameter best manages to reduce it.

4.2.1. Extinction

To study the influence of extinction, we corrected the SFRs using the Calzetti et al. (2000) extinction curve ($A_{FUV}/A_V = 2.54$ and $A_{H\alpha}/A_V = 0.82$). The optical extinction was derived from the Balmer decrement.[17], as measured from spectra of the H II regions. No correction was applied in the MIR regime. The results are presented in Table 17.

We see that the scatter in the extinction correction is stable among the intergalactic star-forming regions in Stephan's Quintet, but increases in NGC 5291, as already mentioned by Boquien et al. (2007), and in NGC 7252. On average, however, when a significant reduction of the relative scatter is observed (which is the case only for debris without older stars), it is comprised between ~30% and ~70%. Given these results, we cannot claim that the extinction is the main parameter governing the discrepancies between the measures of SFR(Hα), SFR(NUV), and SFR(8.0).

Figure 19 plots the ratio of the SFR(8.0) over SFR(FUV) as a function of extinction. We are only including regions with equivalent SFR exceeding 0.02 $M_\odot$ yr^{-1} in order to ensure that the measure of the Balmer decrement, and thus of the extinction, is reliable. The correlation between SFR(8.0)/SFR(FUV) and A_V is weak. The reduction of the scatter mentioned above is largely due to the regions most affected by extinction, such as SQ-B in Stephan's Quintet, where A_V ~3.0 magnitudes.

4.2.2. Metallicity

The nonlinearity of the correlation between the 8.0 μm flux and metallicity, measured by Calzetti et al. (2007) is largely due to the dependence of the PAH emission on metallicity. The collisional debris show, however, a rather restricted range of oxygen abundance: 12 + log(O/H) = 8.3–8.9, close to solar. Why the metallicity in regions located far away from their parent galaxies is on average so high and so uniform remains to be explained. Nevertheless, as far as SF is concerned, it means that the IRAC 8.0 μm traces the SFR linearly. The narrow range of relatively high metallicities should therefore not increase the scatter of the ratio of SFR(8.0)/SFR(FUV).

[17] NGC 7252 and Stephan Quintet are not published yet For Arp 105, Arp 245, NGC 5291 and VCC 2062 refer to Duc & Mirabel (1994), Duc et al. (2000), Duc & Mirabel (1998), and Duc et al. (2007).

Table 17
Ratio of the SFRs Δ (SFR (8.0) /SFR (FUV)) /⟨SFR (8.0) /SFR (FUV)⟩ and Δ (SFR (Hα) /SFR (FUV)) /⟨SFR (Hα) /SFR (FUV)⟩ Raw and Corrected for the Extinction

System	$\langle A_V \rangle$	$\frac{\Delta A_V}{\langle A_V \rangle}$	$\frac{\Delta(\mathrm{SFR(8.0)/SFR(FUV)})}{\langle \mathrm{SFR(8.0)/SFR(FUV)} \rangle}$	$\left(\frac{\Delta(\mathrm{SFR(8.0)/SFR(FUV)})}{\langle \mathrm{SFR(8.0)/SFR(FUV)} \rangle}\right)_{\mathrm{corr.}}$	$\frac{\Delta(\mathrm{SFR(H\alpha)/SFR(FUV)})}{\langle \mathrm{SFR(H\alpha)/SFR(FUV)} \rangle}$	$\left(\frac{\Delta(\mathrm{SFR(H\alpha)/SFR(FUV)})}{\langle \mathrm{SFR(H\alpha)/SFR(FUV)} \rangle}\right)_{\mathrm{corr.}}$
Stephan's Quintet	1.2	0.7	1.3	1.3	0.8	0.8
NGC 5291	0.2	0.8	0.7	1.0	0.3	0.4
NGC 7252	1.6	0.4	0.7	1.3	1.2	1.4
Debris with older stars	1.4	0.4	0.5	0.7	0.8	1.0
Debris without older stars	0.4	1.2	1.5	1.0	2.0	0.6

Note. Only regions having a SFR of at least 0.02 $M_\odot$ yr^{-1} have been selected.

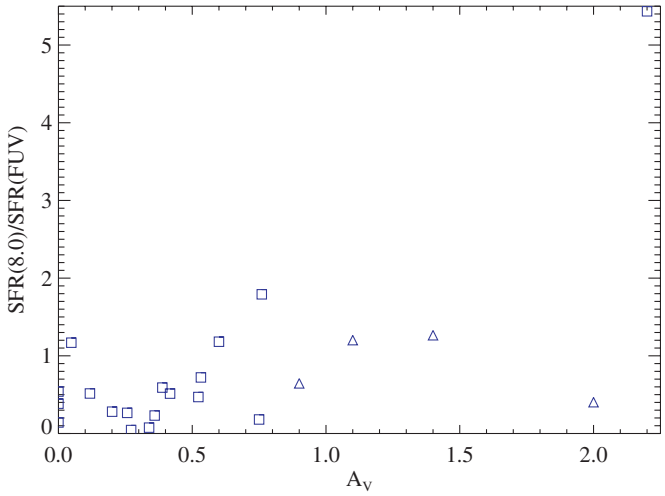

Figure 19. Variation of the SFR(8.0)/SFR(FUV) ratio as a function of A_V. Intergalactic star-forming regions are sorted in two categories whether they contain a significant old stellar population (blue triangle) or are located within mainly gaseous streams (blue square). Only regions having a SFR of at least 0.02 $M_\odot$ yr^{-1} have been selected. The extinctions have been deduced from spectroscopic observations making use of the Balmer decrement except for NGC 5291 where both the Balmer decrement and H I column density have been used (see Boquien et al. 2007, for details).

(A color version of this figure is available in the online journal.)

4.2.3. Stellar Populations

The calibration between the UV/Hα/MIR luminosities and the SFRs, and thus their relative ratio, strongly depends on the age of the most recent starburst as well as on the current and past SF history. Boquien et al. (2007) have shown that the strong scatter of the UV to Hα luminosity ratios, measured along the collisional ring of NGC 5291, and globally its UV excess, were mainly due to age effects: for an instantaneous young starburst, the UV/Hα ratio increases quickly with time, so that small delays between the onset of SF along the ring will induce rapid changes in the UV/Hα ratio.

The relative fraction of young to old stars in a given region may affect the UV to SFR calibration as well, since not only young massive stars emit UV radiation. Thus variations of the UV to Hα ratio may partially reflect contamination of the UV by a substantially older stellar population. To check this, we have distinguished in all our comparison plots (Figures 17–19) collisional debris clearly dominated by old stars pulled out from the parent galaxies (e.g., Arp 105N, Arp 245N) to those apparently formed in pure gaseous tails (Arp 105S, NGC 5291, VCC 2062) and hence made almost exclusively of young stars. The former seem to be UV deficient (but also to have larger extinction) as we can see in Table 15. This shows that significant UV contamination by an older stellar population is unlikely.

Finally, the Initial Mass Function will also affect the value deduced for the SFR. A top heavy IMF will boost the emission due to massive stars, and lead to overestimating the total SFR, if measured on the basis of Hα luminosity. However, as the collision debris are a low-density environment such an IMF would be unexpected (Krumholz & McKee 2008). It would require full analysis of the spectral energy distribution of tidal debris over a broad wavelength range, and not only the three SF tracers listed here, to draw more definitive conclusions. This is beyond the scope of this paper.

4.3. Star Formation and Environment

As noted before, the discrepancies between the different SFR indicators indicate variations of the local properties of star-forming regions. We measure some scatter from one intergalactic region to another. This is, however, similar to what is observed in individual star-forming regions of a single galactic disk. Besides, the MIR to UV ratio is on average similar in the collisional debris and in spiral disks *of the same metallicity*. More generally, despite the differences in the large-scale environments, it is remarkable that intergalactic and galactic regions look so similar, at least when studied via the three main SF diagnostics. The presence of strong PAH features in the collisional debris perfectly illustrates this.

5. CONCLUSIONS

We have studied SF within collisional debris of galaxy–galaxy interactions, including Tidal Dwarf Galaxies and compared it to that occurring in regular spiral galaxies. About 60 star-forming regions in six interacting systems showing prominent SF (with integrated current intergalactic SFR that can reach more than one solar mass per year and half of them comprising more than 20% of that of the whole system) were selected. We used three SF tracers: the UV, measured from PI and archive images from *GALEX*, Hα from ground-based Fabry-Perot and narrowband images and MIR emission from IRAC on *Spitzer*. We also present two new spectroscopic observations in the MIR with the *Spitzer*/IRS instrument in addition to those published by Higdon et al. (2006). We have obtained the following results.

1. Dust emission in tidal debris, as probed with broadband images and spectra is at a level similar to that encountered in star-forming regions of comparable metallicity and luminosity in galaxies of a comparison sample.
2. The SFR inferred from UV, Hα, and MIR show similar trends and scatter as compared to classical star-forming regions in galaxies.

3. Extinction and metallicity are not the main parameters governing the scatter in the properties of intergalactic star-forming regions. Age effects, and variations in the stellar populations, seem to play a dominant role.

The similarity of the SF properties in intergalactic star-forming regions and within spiral galaxies leads us to conclude that SF processes seem to be mainly driven by local properties—gas column density, dust content, etc.—rather than by large-scale environmental factors. SF may proceed in intergalactic space the same way as in spiral disks. As a result, intergalactic star-forming regions may be used as a laboratory to study SF: results obtained on intergalactic star-forming regions can be applied to star-forming regions in galaxies in general, provided the metallicity is similar. The main advantage of the latter environment is its simplicity: the individual star-forming regions are physically isolated, simplifying flux measurements. Moreover, it is worth remembering that the influence of shocks, magnetic fields, etc. is much reduced in the intergalactic medium.

The absence of an old stellar component in at least a fraction of collisional debris makes any analysis of their Spectral Energy Distribution less degenerate, giving hope to constrain key parameters, such as the Initial Mass Function. A variation of the IMF in extreme environments is actively discussed in the literature: in the outermost low density star-forming regions in spirals (Krumholz & McKee 2008; Pflamm-Altenburg & Kroupa 2008) as well as in ultracompact dwarf galaxies (Mieske & Kroupa 2008). Other strongly debated questions, such as the threshold for SF in gas clouds and the SF efficiency, may be addressed using collisional debris. We are presently collecting a large photometric database to investigate these questions in tidal dwarf galaxies. They will be addressed in future papers.

This research has made use of the NASA/IPAC Extragalactic Database (NED) which is operated by the Jet Propulsion Laboratory, California Institute of Technology, under contract with the National Aeronautics and Space Administration.

GALEX is a NASA Small Explorer, launched in 2003 April. We gratefully acknowledge NASA's support of the construction, operation, and science analysis for the *GALEX* mission, developed in cooperation with the Centre national d'études spatiales, France, and the Korean Ministry of Science and Technology.

Based on observations obtained at the Canada-France-Hawaii Telescope (CFHT) which is operated by the National Research Council of Canada, the Institut National des Sciences de l'Univers of the Centre National de la Recherche Scientifique of France, and the University of Hawaii.

M.B. acknowledges support by NASA-ADP grant NNX07AN90G and D. Calzetti for fruitful discussions. U.L. acknowledges financial support by the Spanish Science Ministry under grant AYA2007-67625-C02-02 and by the Junta de Andalucía. V.C. would like to acknowledge partial support from EU ToK grant 39965. Finally, we also thank the referee for useful comments.

Facilities: CAO:2.2 m, CFHT, ESO:3.6 m, *GALEX*, KPNO:2.1 m, NTT, *Spitzer*.

REFERENCES

Appleton, P. N., et al. 2006, ApJ, 639, L51
Asplund, M., Grevesse, N., & Sauval, A. J. 2005, in ASP Conf. Ser. 336, Cosmic Abundances as Records of Stellar Evolution and Nucleosynthesis, ed. T. G. Barnes, III & F. N. Bash (San Francisco, CA: ASP), 25
Bicker, J., & Fritze-v. Alvensleben, U. 2005, A&A, 443, L19
Boquien, M., Duc, P. A., Braine, J., Brinks, E., Lisenfeld, U., & Charmandaris, V. 2007, A&A, 467, 93
Bournaud, F., Duc, P. A., Amram, P., Combes, F., & Gach, J. L. 2004, A&A, 425, 813
Bournaud, F., et al. 2007, Science, 316, 1166
Braine, J., Duc, P. A., Lisenfeld, U., Charmandaris, V., Vallejo, O., Leon, S, & Brinks, E. 2001, A&A, 378, 51
Braine, J., & Herpin, F. 2004, Nature, 432, 369
Braine, J., Lisenfeld, U., Duc, P. A., & Leon, S. 2000, Nature, 403, 867
Calzetti, D., Armus, L., Bohlin, R. C., Kinney, A. L., Koornneef, J., & Storchi-Bergmann, T. 2000, ApJ, 533, 682
Calzetti, D., et al. 2005, ApJ, 633, 871
Calzetti, D., et al. 2007, ApJ, 666, 870
Cao, C., & Wu, H. 2007, AJ, 133, 1710
Cohen, M., Megeath, S. T., Hammersley, P. L., Martín-Luis, F., & Stauffer, J. 2003, AJ, 125, 2645
Cortese, L., Gavazzi, G., Boselli, A., Franzetti, P., Kennicutt, R. C., O'Neil, K., & Sakai, S. 2006, A&A, 453, 847
Dale, D. A., et al. 2007, ApJ, 655, 863
de Grijs, R., Lee, J. T., Mora Herrera, M. C., Fritze-v. Alvensleben, U., & Anders, P. 2003, New Astron., 8, 155
Duc, P. A., Braine, J., Lisenfeld, U., Brinks, E., & Boquien, M. 2007, A&A, 475, 187
Duc, P. A., Brinks, E., Springel, V., Pichardo, B., Weilbacher, P., & Mirabel, I. F. 2000, AJ, 120, 1238
Duc, P. A., Brinks, E., Wink, J. E., & Mirabel, I. F. 1997, A&A, 326, 537
Duc, P. A., & Mirabel, I. F. 1994, A&A, 289, 83
Duc, P. A., & Mirabel, I. F. 1998, A&A, 333, 813
Elmegreen, B. G., & Efremov, Y. N. 1996, ApJ, 466, 802
Engelbracht, C. W., Gordon, K. D., Rieke, G. H., Werner, M. W., Dale, D. A, & Latter, W. B. 2005, ApJ, 628, L29
Engelbracht, C. W., Rieke, G. H., Gordon, K. D., Smith, J. T, Werner, M. W, Moustakas, J., Willmer, C. N. A., & Vanzi, L. 2008, ApJ, 678, 804
Gil de Paz, A., et al. 2005, ApJ, 627, L29
Gil de Paz, A., et al. 2007, ApJS, 173, 185
Gordon, K. D., Engelbracht, C. W., Rieke, G. H., Misselt, K. A., Smith, J. T., & Kennicutt, Jr., R. C. 2008, ApJ, 682, 336
Hancock, M., Smith, B. J., Struck, C., Giroux, M. L., Appleton, P. N, Charmandaris, V., & Reach, W. T. 2007, AJ, 133, 676
Hibbard, J. E., Guhathakurta, P., van Gorkom, J. H., & Schweizer, F. 1994, AJ, 107, 67
Hibbard, J. E., & Mihos, J. C. 1995, AJ, 110, 140
Higdon, S. J., Higdon, J. L., & Marshall, J. 2006, ApJ, 640, 768
Higdon, S. J. U., et al. 2004, PASP, 116, 975
Houck, J. R., et al. 2004, ApJS, 154, 18
Jog, C. J., & Solomon, P. M. 1984a, ApJ, 276, 114
Jog, C. J., & Solomon, P. M. 1984b, ApJ, 276, 127
Kennicutt, R., et al. 2007, BAAS, 39, 894
Kennicutt, Jr., R. C. 1998, ARA&A, 36, 189
Kennicutt, Jr., R. C., et al. 2003, PASP, 115, 928
Krumholz, M. R., & McKee, C. F. 2008, Nature, 451, 1082
Lin, C. C., & Shu, F. H. 1964, ApJ, 140, 646
Lisenfeld, U., Braine, J., Duc, P. A., Brinks, E., Charmandaris, V., & Leon, S. 2004, A&A, 426, 471
Lisenfeld, U., Braine, J., Duc, P. A., Leon, S., Charmandaris, V., & Brinks, E. 2002, A&A, 394, 823
López-Sánchez Á, R., Esteban, C., & Rodríguez, M. 2004, ApJS, 153, 243
Madden, S. C., Galliano, F., Jones, A. P., & Sauvage, M. 2006, A&A, 446, 877
Mendes de Oliveira, C., Cypriano, E. S., Sodré, Jr., L., & Balkowski, C. 2004, ApJ, 605, L17
Mieske, S., & Kroupa, P. 2008, ApJ, 677, 276
Pahre, M. A., Ashby, M. L. N., Fazio, G. G., & Willner, S. P. 2004, ApJS, 154, 235
Pérez-González, P. G., et al. 2006, ApJ, 648, 987
Pflamm-Altenburg, J., & Kroupa, P. 2008, Nature, 455, 641
Rosenberg, J. L., Ashby, M. L. N., Salzer, J. J., & Huang, J. S. 2006, ApJ, 636, 742
Ryan-Weber, E. V., et al. 2004, AJ, 127, 1431
Schweizer, F. 1978, in IAU Symp. 77, Structure and Properties of Nearby Galaxies, ed. E. M. Berkhuijsen & R. Wielebinski (Dordrecht: Kluwer), 279
Smith, B. J., Struck, C., Hancock, M., Appleton, P. N., Charmandaris, V., & Reach, W. T. 2007, AJ, 133, 791
Smith, B. J., et al. 2008, AJ, 135, 2406
Struck, C. 1997, ApJS, 113, 269
Struck, C. 2007, in IAU Symp. 237, Triggered Star Formation in a Turbulent ISM, ed. B. G. Elmegreen & J. Palous (Dordrecht: Kluwer), 317

Thilker, D. A., et al. 2005, ApJ, 619, L79
Toomre, A. 1964, ApJ, 139, 1217
Walter, F., et al. 2007, ApJ, 661, 102
Weilbacher, P. M., Duc, P. A., & Fritze-v. Alvensleben, U. 2003, A&A, 397, 545
Werk, J. K., Putman, M. E., Meurer, G. R., Oey, M. S., Ryan-Weber, E. V, Kennicutt, Jr., R. C., & Freeman, K. C. 2008, ApJ, 678, 888
Wu, H., Cao, C., Hao, C. N., Liu, F. S., Wang, J. L., Xia, X. Y., Deng, Z. G, & Young, C. K. S. 2005, ApJ, 632, L79
Wu, Y., Charmandaris, V., Hao, L., Brandl, B. R., Bernard-Salas, J., Spoon, H. W. W., & Houck, J. R. 2006, ApJ, 639, 157
Xu, C., Sulentic, J. W., & Tuffs, R. 1999, ApJ, 512, 178
Xu, C. K., et al. 2005, ApJ, 619, L95
Zwicky, F. 1956, Ergebnisse der exakten Naturwissenschaften, 29, 344